

Supplementary Information

Derivations

We derived the elastic modulus and the viscosities of the viscoelastic model as laid out in previous work,¹ with adaptations for a rectangular channel and our chosen model. The Jeffreys model consists of three elements: a dashpot in series with a Kelvin-Voigt element, i.e., a spring and a dashpot in parallel. For this model, the creep is described by the following equation:

$$L(t) = \frac{f}{k} \left(1 - e^{-t/\tau}\right) + \frac{f}{\mu} t$$

Where f is the force, k is the spring constant, τ is the relaxation time ($\tau = \frac{k}{\mu}$) and μ is the viscosity of the dashpot in series. At short time scales, the first term dominates, resulting in a rapidly rising curve, while at long time scales, the second term dominates, leading to a linear regime.

The aspiration force is given by:

$$f = \pi R_p^2 \Delta P$$

Where R_p is the radius of the micropipette and ΔP is the applied pressure.

At short time scales, the force is balanced by the elastic deformation and is given by the following equation:

$$\frac{f}{A} = CE \frac{\delta}{R_p}$$

Where A is the cross-sectional area of the pipette, C is approximately equivalent to 1,¹ E is the elastic modulus and δ is the elastic deformation at short times. We thus obtain $f = \pi R_p E \delta$.

The definition of the spring constant (k) is the relationship between the force and the extension: $f = k \times \delta$, and thus $\frac{f}{\delta} = k = \pi R_p E$.

At long time scales, the force is balanced by viscous flow. The dissipative force due to the plug at the entrance of the capillary is given by the following equation:

$$f = 3\pi^2 \eta R_p \frac{dL}{dt}$$

Where μ is the viscosity and R_p is the radius of the pipette. At long time scales, the second term of equation 1 dominates and we obtain: $\frac{dL}{dt} = \frac{f}{\mu}$, thus $\mu = \frac{f}{dL/dt} = 3\pi^2 \eta R_p$

Inserting these expressions into equation 1, we obtain the following:

$$L(t) = \frac{f}{k} \left(1 - e^{-t/\tau}\right) + \frac{f}{\mu} t = \frac{\pi R_p^2 \Delta P}{\pi R_p E} \left(1 - e^{-\frac{E}{3\pi\eta} t}\right) + \frac{\pi R_p^2 \Delta P}{3\pi^2 \eta R_p} t = \frac{R_p \Delta P}{E} \left(1 - e^{-\frac{E}{3\pi\eta} t}\right) + \frac{R_p \Delta P}{3\pi\eta} t$$

We use equations 7 and 19 of Son² to obtain a correction for rectangular constrictions. We therefore obtain the following effective radius:

$$R_{eff}^4 = \frac{2}{\pi} \frac{W \times H^3}{(1 + H/W)^2 \times f^*}$$

Where H and W are the dimensions of the cross-section of the channel with $H < W$; and f is a function given by Son.²

We thus obtain:

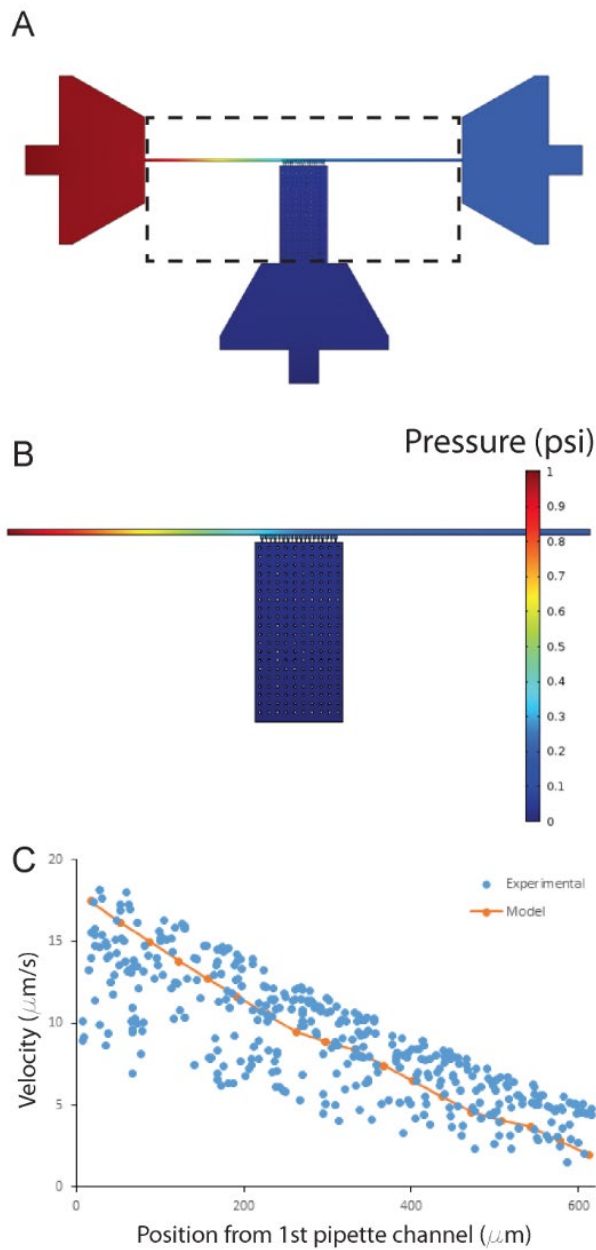
$$L(t) = \frac{R_{eff}\Delta P}{E} \left(1 - e^{-\frac{E}{3\pi\eta}t} \right) + \frac{R_{eff}\Delta P}{3\pi\eta} t$$

By fitting the data to this function, we obtain values for the elastic modulus and the viscosities.

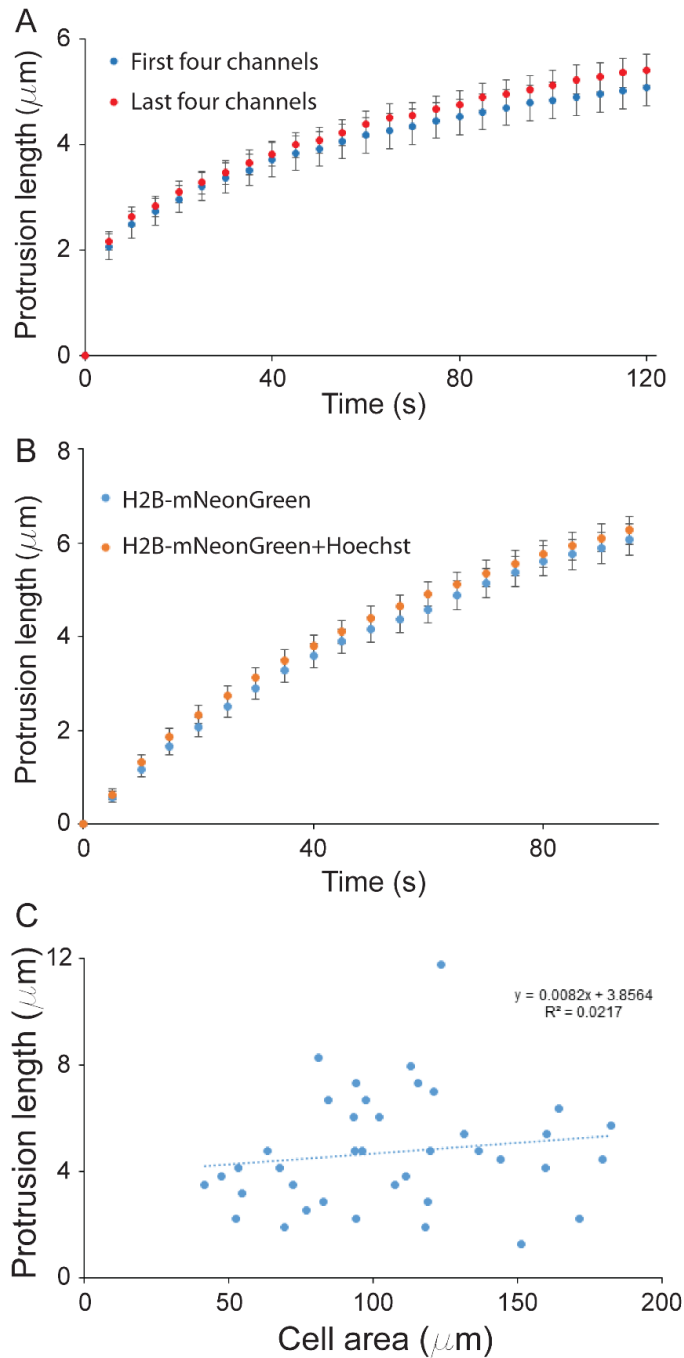
References

- 1 K. Guevorkian, M. J. Colbert, M. Durth, S. Dufour and F. Brochard-Wyart, *Phys. Rev. Lett.*, 2010, **104**, 1–4.
- 2 Y. Son, *Polymer*, 2007, **48**, 632–637.

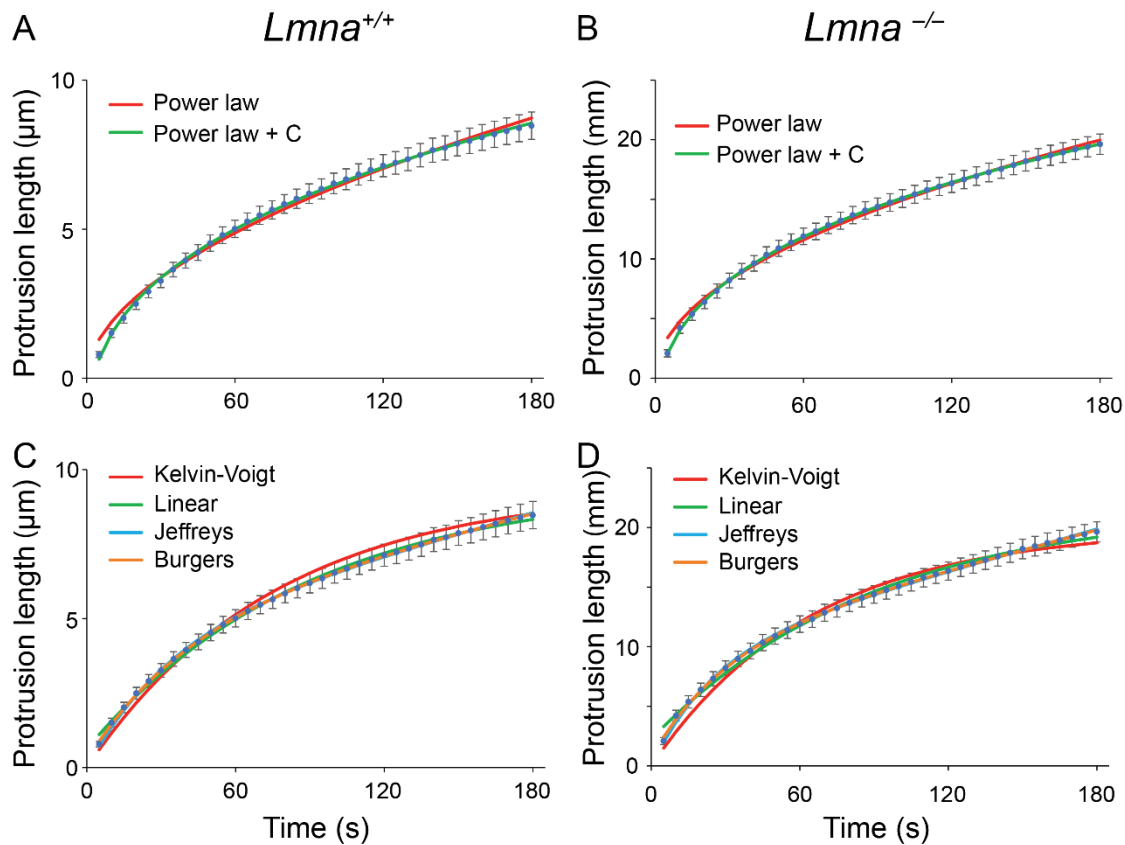
Supplementary Figures



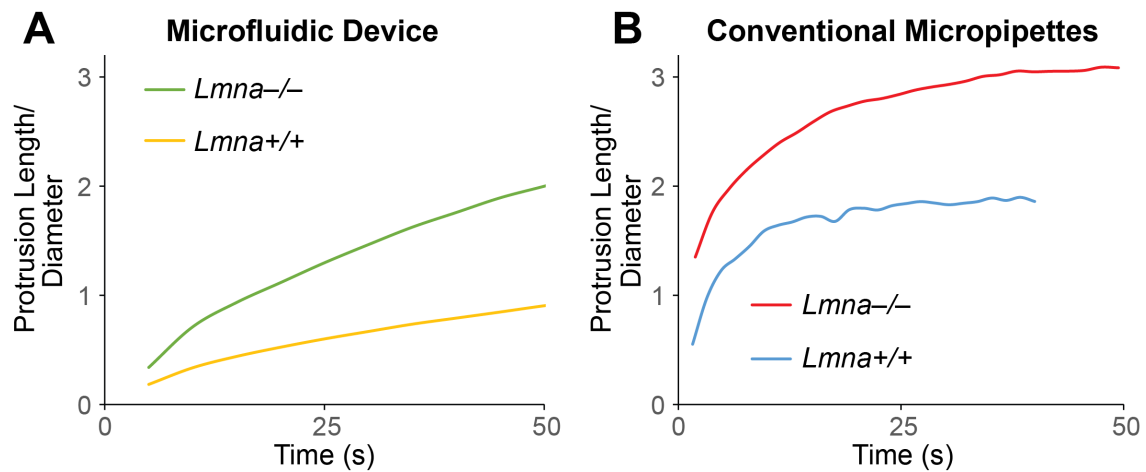
Supplementary Figure 1: Simulation on micropipette channels in “open” configuration. (A) Overview of the simulated pressure distribution in the entire microfluidic device. (B) Close-up of the area containing the micropipette channels (area surrounded by dashed line in panel A) showing a rapid decrease of the pressure upstream of the micropipette channels. (C) Comparison of the velocity obtained from the simulation (orange line) and measured velocities obtained from the streak length of fluorescent beads in the microfluidic device (blue points).



Supplementary Figure 2. Effect of microchannel position, Hoechst labeling, and cell size on nuclear deformation measurements. (A) The deformation rate as a function of microchannel position. We compared the deformation rate of MDA-MB-231 cells in the first four and last four micropipette channels. Similar to the results shown in Figure 3C, the position of the cells does not have a significant influence on the deformation rate of the cells. **(B)** Effect of a DNA intercalating agent on the deformability measurements. The deformability of cells was not significantly different when Hoechst 33342 was added at the concentrations we use in our experiments. **(C)** Effect of nuclear size on deformability of the nucleus. We compared the cross-sectional area and the protrusion length at 60 s in individual cells. Using a regression analysis, we determined that the slope of the linear regression (0.008) was smaller than the 95% confidence interval (0.018) associated with it, indicating that the slope is not significantly different from 0.



Supplementary Figure 3. Comparison of the models used to fit the data. (A, B) The data was fit with a simple power law ($y = A t^\alpha$) and a power law with an additional constant ($y = A t^\alpha + C$) to account for error in the first time point. The simpler model does not follow the data well at small time points due to the uncertainty in time zero, resulting in a flattening of the curve and thus a large change in the exponent value. The second model is a better fit at short time points. (C, D) The four viscoelastic (spring and dashpot) models. The Kelvin-Voigt and Standard Linear Solid models include a spring in parallel and thus do not result in a viscous linear increase with time. We thus didn't chose these models as our data increases linearly at long time points (indicative of a dashpot in series). The Jeffreys model is made up of a dashpot in series with a Kelvin-Voigt element and thus is the simplest element to accurately describe our data. Accordingly, the R^2 values are smaller for the Jeffreys model than the first two models. (See Supplemental Table 1.) The Burgers model includes an additional element, and consequently exhibits a better fit, but is only a minimal improvement.



Supplementary Figure 4: Comparison of the deformation of MEFs in microfluidic and conventional micropipettes. (A) Protrusion length of the nuclei, normalized to the effective diameter, as a function of time. (B) Nuclear protrusion length in conventional micropipettes over time, normalized to the micropipette diameter measured as the width of the maximal nuclear protrusion. The two sets of data show the same trend: lamin A/C-deficient (*Lmna*^{-/-}) nuclei are more deformable than wild-type (*Lmna*^{+/+}) nuclei.

Supplementary Tables

Model	# of variables	<i>Lmna</i> ^{+/+}		<i>Lmna</i> ^{-/-}	
		<i>R</i> ²	Residuals	<i>R</i> ²	Residuals
Power law	2	0.99345	1.1	0.99520	3.7
Power law with C	3	0.99941	0.11	0.99989	0.13
Kelvin-Voigt	2	0.99401	2.4	0.98903	13
Linear	3	0.99800	0.32	0.99639	3.9
Jeffreys	3	0.99963	0.082	0.99921	0.68
Burgers	4	0.99980	0.031	0.99941	0.37

Supplementary Table 1: Values of the Coefficient of Determination (*R*²) and residuals calculated for lamin A/C-deficient (*Lmna*^{-/-}) and wild-type (*Lmna*^{+/+}) MEFs for each model.

Parameter	<i>Lmna</i> ^{+/+} MEFs	<i>Lmna</i> ^{-/-} MEFs	Ratio of <i>Lmna</i> ^{+/+} / <i>Lmna</i> ^{-/-}
E (kPa)			
Conventional micropipette	2.5 ± 0.5 (<i>n</i> =6)	1.6 ± 0.2 (<i>n</i> =10)	1.6
Microfluidic device	2.2 ± 0.1 (<i>n</i> =58)	1.2 ± 0.1 (<i>n</i> =39)	1.9
μ₁ (kPa*s)			
Conventional micropipette	1.1 ± 0.2 (<i>n</i> =6)	0.6 ± 0.1 (<i>n</i> =10)	1.8
Microfluidic device	8 ± 1 (<i>n</i> =58)	3.9 ± 0.4 (<i>n</i> =42)	2.2
μ₂ (kPa*s)			
Conventional micropipette	22 ± 5 (<i>n</i> =3)	17 ± 4 (<i>n</i> =7)	1.3
Microfluidic device	70 ± 10 (<i>n</i> =70)	29 ± 3 (<i>n</i> =35)	2.4

Supplemental Table 2. Comparison of parameters obtained using conventional micropipettes and microfluidic micropipettes. Viscoelastic parameters were obtained by fitting a Kelvin-Voigt to data obtained from experiments on *Lmna*^{+/+} and *Lmna*^{-/-} MEFs using conventional micropipette aspiration or the microfluidic device system. Values were obtained by fitting the curve obtained from each nucleus separately and removing the outliers (defined as fits that were equivalent to a straight line, i.e., the relaxation time in equation 4 was equal to zero, and parameters that were greater than 1.5-times the 75th percentile). Parameter values are listed as mean ± s.e.m.

Supplemental Movies

Movie 1: Overview of the microfluidic micropipette devices. Demonstration of a typical experiment, in which the cells in the microchannels are cleared by applying a positive pressure to the outlet and swept away to the waste (bottom). Upon release of the pressure at the outlet to P_{atm} , new cells flow into the pockets from the cell inlet (top) and are slowly deformed into the micropipette channels. The image sequence on the left depicts the brightfield view, the sequence on the right shows the fluorescence signal of the Hoechst 33342 labeled nuclei. The time stamp indicates MM:SS.

Movie 2: Deformation of wild-type cells. *Lmna*^{+/+} MEFs are deformed into the micropipette channels. The image sequence on the left depicts the brightfield view, the sequence on the right shows the fluorescence signal of the Hoechst 33342 labeled nuclei. The time stamp indicates MM:SS.

Movie 3: Deformation of lamin A/C-deficient cells. *Lmna*^{-/-} MEFs are deformed into the micropipette channels. The image sequence on the left depicts the brightfield view, the sequence on the right shows the fluorescence signal of the Hoechst 33342 labeled nuclei. The time stamp indicates MM:SS.